ACS OMEGA

Open Access

http://pubs.acs.org/journal/acsodf

Article

Bismuth Vanadate and 3D Graphene Composite Photoanodes for Enhanced Photoelectrochemical Oxidation of Water

Abhishek Sharma, Sudipa Manna, Sriram Kumar, and Ashis Kumar Satpati*

Cite This: *ACS Omega* 2023, 8, 33452−33465

Read Online

ACCESS | Metrics & More | Article Recommendations | Supporting Information

ABSTRACT: Bismuth vanadate ($BiVO_4$) has been one of the most promising photoanodes for the photoelectrochemical (PEC) water oxidation process. Efforts are still on to overcome the drawbacks of this photoanode to enhance the catalytic efficiency and improve the stability. In the present work, three-dimensional graphene (3D-G) was incorporated inside the $BiVO_4$ matrix, primarily to improve the conductivity of the material. The photoanodes are fabricated with the incorporation of a SnO_2 heterojunction and application of cobalt borate ($Co-B_i$) as a cocatalyst. The incorporation of 3D-G has enhanced the photocurrent from 0.72 o 1.21 mA cm^{-2} in ITO/SnO_2/$BiVO_4$ and ITO/SnO_2/3D-G-$BiVO_4$ materials; the photocurrent has been improved from 0.89 to 1.52 mA cm^{-2} in ITO/SnO_2/$BiVO_4$/$Co-B_i$ and ITO/SnO_2/3D-G-$BiVO_4$. Semiconductor properties are evaluated from the Mott−Schottky measurements, and the charge transfer and transport kinetics of the PEC process are measured from several photoelectrochemical investigations. Both the charge transport and the charge transfer efficiencies are enhanced upon inclusion of 3D-G into the catalyst system. The lifetime of the charge carrier is observed to be increased. The decrease in the decay kinetics of the holes, enhancement in the open-circuit photovoltage (OCPV), and the resulting modulation of the surface states are responsible for the enhancement in the surface charge transfer process due to the inclusion of 3D-G into the catalytic system. Therefore, the additional role of 3D-G in the modulation of the surface states and release of the Fermi level pinning has made the band alignment between the semiconductor and the analyte better, which resulted in enhanced catalytic performance in the photoelectrochemical oxidation of water.

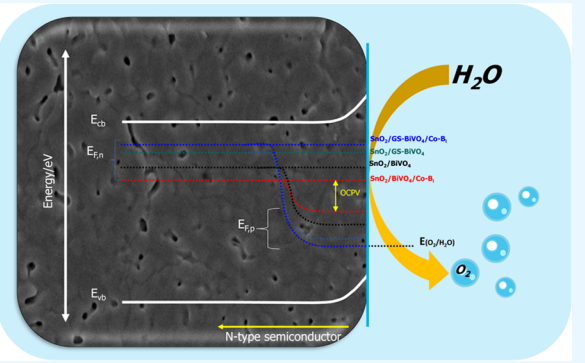

1. INTRODUCTION

Generation of hydrogen using solar energy is one of the promising routes to harvest solar energy for sustainable utilization of renewable energy. The photoelectrochemical (PEC) splitting of water using solar light is the most promising route to harvest solar energy for sustainable energy generation with zero carbon footprints.[1] The overall water splitting reaction through the PEC route has the anodic process; the oxygen evolution reaction (OER) and the cathodic process; and the hydrogen evolution reaction (HER). However, the sluggish kinetics through complicated pathways makes the oxygen evolution reaction the rate-limiting step of the overall water splitting process. The development of an efficient photoanode for sustainable oxidation of water is therefore the most challenging in the overall PEC water splitting. The important photoanode materials that have been investigated over the years are TiO_2, WO_3, α-Fe_2O_3, and $BiVO_4$,[2−6] and most of these materials are not so expensive for practical utilizations. Among them, $BiVO_4$ has been extremely promising due to some of the important parameters such as band gap ∼2.4 eV, favorable band position, photoelectrochemical stability in aqueous solution, earth abundance, and nontoxicity with a high theoretical efficiency of 7.5 mA cm^{-2} under AM 1.5 G illuminations.[7] However, the experimentally observed solar to hydrogen (STH) conversion efficiency of the bare $BiVO_4$ is only 5.2%; such lowering of experimental efficiency arises mainly due to the slow surface kinetics, poor hole diffusion, and fast charge recombination.[8−13]

Several strategies have been adopted to enhance the experimental STH efficiency, which include heterojunction formation,[14−18] heteroatom doping,[6,19,20] creation of oxygen vacancies,[21,22] band engineering,[20,23−26] crystal facet engineering,[27−29] and nanostructure control;[30] all these processes are essentially aimed at enhancing the transport of the photogenerated holes from the bulk of the material to the interface. Heterojunction formation with suitable band positions has a specific role in transporting the majority carriers toward the sink through the generation of low-energy pathways, which

Received: May 10, 2023
Accepted: August 30, 2023
Published: September 9, 2023

reduces the electron−hole recombination. The sluggish OER kinetics at the interface and the associated trapped surface states cause the significant decrease in overall efficiency.[31,32] Surface modification using oxygen evolution catalysts (OECs) has been designed for the acceleration of the surface hole transfer kinetics of $BiVO_4$-based photoanodes. The OEC catalysts such as Co−P_i,[19,33−35] Co−B_i,[36−38] NiOOH/Ni-borate,[39] FeOOH,[24] Ni(Fe)OOH,[25] and FeOOH/NiOOH[7] have been investigated to improve the onset potential and suppress the charge recombination for the PEC water oxidation. Among the different OECs, the Co-based cocatalyst, especially cobalt borate (Co−B_i), has been extensively investigated in view of its superior catalytic activity in PEC water oxidation.[40] The enhancement of both the bulk and surface charge movements, which are called charge transport and charge transfer, respectively, through the modifications of the catalytic composite materials is therefore the important aspect to be worked on.

The carbon nanostructures have important roles in the electrochemical catalysis processes. The one-dimensional nanomaterial with sp^2-bonded carbon in the form of carbon nanotubes (CNTs) is highly popular due to the enhanced conductivity and edge adsorption properties. The two-dimensional (2D) form of carbon as a graphene sheet has been in the spotlight since its discovery in 2004.[41] In the graphene sheet with the presence of sp^2 carbon in the honeycomb-like arrangements in a single plane, the material has one of the highest specific surface areas. The long-range $\pi-\pi$ stacking has resulted in several interesting properties; most importantly, the excellent electron mobility is of the primary interest for its use as a catalyst and as the catalyst support. The excellent thermal conductivity of graphene is also helpful in designing the catalyst support, as the material network would distribute the localized heat generated during the catalysis process. In spite having such good properties, when the 2D graphene is put on practical applications in energy harvesting and storage, it finds difficulty in sustainability due to the restacking of the graphene sheets.[42−45]

The alternate way to solve the issue is to construct three-dimensional (3D) interconnected structures in place of the 2D structure. The 3D structure essentially retains the goodness of the graphene network in addition to providing stability in the system. The 3D graphene (3D-G) nanostructures are generated through several synthesis protocols, and the performance of the materials varies with the variation in the synthesis protocols. The definition of the 3D graphene and differentiating it from the graphite originate from the involvement of a number of graphene layers and 3D structuring of the graphene sheets from the two-dimensional form. Presently, 3D graphene has been synthesized with graphene oxide (GO) as the starting material. $BiVO_4$ is entangled with the 3D-G matrix to generate the $BiVO_4$/3D-G composite-modified photoanode. The modification of the PEC catalytic performances is discussed in the direction of enhancement of the conductivity of the material, essentially to drive the charge carrier in both the directions.

In some of our previous publications, we have tried to improve the catalytic performance of $BiVO_4$ through the formation of a SnO_2 heterojunction, doping with Mo, treatments by photocharging, and enhancement of the catalytic performance by generation of the electrocatalyst Co−B_i outer layer.[6,35] The photocorrosion aspects of $BiVO_4$ have been reduced by generation of the TiO_2 surface protective layer using the atomic layer deposition technique.[46] In addition to the enhancement of the stability of $BiVO_4$, the TiO_2 surface layer is observed to enhance the catalytic performance. The present work has been focused on the enhancement of the conductivity of $BiVO_4$ through the incorporation of 3D-G into the $BiVO_4$ matrix. In addition to providing conductivity, the 3D-G matrix has the ability to hold the $BiVO_4$ for enhanced stability and also to channelize the charges for better catalytic performances and enhance both the charge transfer and transport processes. The 3D-G network is expected to provide the required electronic stability of the composite without any detrimental effect on the performance.

2. MATERIALS AND METHODS

2.1. Materials. Bismuth(III) nitrate (Bi $(NO_3)_3{\cdot}5H_2O$, 98%), ammonium vanadate (NH_4VO_4, >99%), stannic chloride ($SnCl_4$, 98%), sodium sulfite (Na_2SO_3, 98%), and cobalt(II) nitrate hexahydrate ($Co(NO_3)_2{\cdot}6H_2O$, ≥98%) were purchased from Sigma-Aldrich. Sodium sulfate (Na_2SO_4), sodium hydroxide (NaOH, 98%), and boric acid (H_3BO_3, 98%) were obtained from Sarabhai M Chemicals. Ethylene glycol (EG) and potassium ferricyanide were purchased from SD fine Chemicals Limited. All the chemicals were used without any further purification. Indium-doped tin oxide (ITO) was used as a transparent substrate for the thin film fabrication.

2.2. Fabrication of the Photoanode. The $SnO_2/BiVO_4$ heterojunction was prepared by a previously reported method.[6] Briefly, 0.2 M $SnCl_4$ in EG was stirred overnight and a 100 μL aliquot was spin-coated onto ITO at 2000 rpm for 30s and dried at 200 °C for 5 min. The 8 cycles of spin coating were performed followed by 2 h of annealing at 450 °C (heating rate was kept 5 °C per min). These modified electrodes are named as ITO/SnO_2. These ITO/SnO_2 electrodes were further spin-coated in a similar fashion with bismuth vanadate precursor solution, which was prepared by dissolving 0.2 M bismuth nitrate and 0.2 M ammonium vanadate in a 4:1 ethylene glycol/water mixture. 3D-G was prepared from GO, 100 mg of GO powder was dispersed into 200 mL of deionized (DI) water, and 4 g of urea was added to the solution at 0 °C under stirring conditions. 200 mL of 0.025 M HCl solution was added and kept under vigorous stirring overnight. The material was collected by centrifuging and redispersed into 100 mL of DI water. 0.5 g of ascorbic acid was added to this mixture and left undisturbed at 100 °C for 6 h. A cylindrical foam structure was formed, and it was lyophilized to obtain the 3D-G. For inclusion of 3D-G, the ITO/SnO_2 electrode was coated with the bismuth vanadate precursor containing thoroughly mixed 1 mg/mL 3D-G. Finally, these electrodes were annealed at 450 °C for 2 h under a nitrogen atmosphere to avoid decomposition of 3D-G, and the samples without 3D-G are annealed under atmospheric conditions. The electrodes with 3D-G are named ITO/SnO_2/3D-G-$BiVO_4$, and those without 3D-G are named as ITO/SnO_2/$BiVO_4$.

To further improve the catalytic activity of the electrodes, photoassisted electrodeposition of cobalt borate (Co−B_i) was performed. The deposition bath was prepared by dissolving 2 mM Co(II) nitrate in 0.1 M borate buffer solution of pH 8. Photoassisted electrodeposition was performed at 0.86 V vs reversible hydrogen electrode (RHE) under 1 sun light irradiated using a solar simulator fitted with an AM 1.5 G filter. The ITO/SnO_2/$BiVO_4$ electrode modified with Co−B_i is named as ITO/SnO_2/$BiVO_4$/Co−B_i, and similarly, the Co−

https://doi.org/10.1021/acsomega.3c03229
ACS Omega 2023, 8, 33452−33465

B_i-deposited electrode corresponding to ITO/SnO_2/3D-G-$BiVO_4$ is named as ITO/SnO_2/3D-G-$BiVO_4$/Co−B_i.

2.3. Instrumentation. X-ray diffraction (XRD) analysis of the prepared samples was performed by using a Rigaku Smartlab instrument with Cu Kα radiation (λ = 1.5406 Å). Raman spectra of the photoanodes were recorded by using a Lab RAM HR 800 Micro laser Raman system with an Ar^+ laser of 516 nm. The morphology of the photoanode materials was examined by field emission scanning electron microscopy (FE-SEM, JEOL model JSM-7600F) and atomic force microscopy (AFM, Nanosurf with C3000 controller). X-ray photoelectron spectroscopy (XPS, MULTI LAB, VG Scientific, Al K_α radiation as a monochromator) was used to investigate the binding energy of the photoanodes. The evolved oxygen gas was determined using a gas chromatography instrument model GC 2010 from Shimadzu. The gas samples are collected using a syringe through a septum after PEC experiments at a constant potential of 1.0 V vs RHE after 30 min of electrolysis. Photoelectrochemical measurements were performed using a Zahner potentiostat fitted with a solar simulator from Sciencetech Inc. The absorption spectra were collected using an Ocean optics UV−Vis spectrophotometer. The incident photon to current efficiency (IPCE) measurements were carried out using a Xe lamp associated with a monochromator from Optosolar, Germany.

2.4. Parameters in Photoelectrochemical (PEC) Measurements. All PEC experiments were carried out under 1 sun light using an AM 1.5 G solar simulator in a CHI 920 D model in a three-electrode setup. Ag/AgCl (3.0 M KCl), Pt wire, and catalyst-coated ITO served as the reference, counter, and working electrodes, respectively. A H-cell was used, and all measurements were done under back illumination. Linear sweep voltammetry (10 mV s^{-1}) and chopped light voltammetry (5 mV s^{-1}) were performed to measure the photocurrent. To understand the surface charge separation ($\eta_{transfer}$) and bulk charge separation ($\eta_{transport}$) efficiencies of the photoanodes, linear sweep voltammetry (LSV) in 0.1 M Na_2SO_3 solution in 0.1 M borate buffer solution (BBS) was performed, and from photocurrent, the efficiency parameters were calculated using the following equations

$$\eta_{transfer} = \frac{J_{H_2O}}{J_{Na_2SO_3}} \times 100\% \quad (1)$$

$$\eta_{transport} = \frac{J_{Na_2SO_3}}{J_{max.}} \times 100\% \quad (2)$$

$$J_{max.} = \frac{\text{integration of light absoption}}{\text{integration of solar light spectrum}} \quad (3)$$

where $J_{max.}$ was calculated from the photocurrent obtained from the silicon detector, J_{H_2O} is the photocurrent density of the water, and $J_{Na_2SO_3}$ is the photocurrent of the oxidation of the sulfite.

IPCE was measured at three different voltages (vs Ag/AgCl) in monochromatic light from 350 to 550 nm (xenon lamp) by using the following equation

$$\text{IPCE \%} = \left(\frac{J\left(\frac{A}{cm^2}\right)}{P_{in}\left(\frac{w}{cm^2}\right)} \times \frac{1240}{\lambda\ (\text{nm})} \right) \times 100\% \quad (4)$$

where J is the photocurrent density, P_{in} is the power of the incident monochromatic light (measured using a silicon-based detector from Newport), and λ is the wavelength in nm.

Absorbed photon to current conversion efficiency (APCE) has also been derived from IPCE and absorbance using the equation

$$\text{APCE} = \text{IPCE}/(1 - 10^{-A}) \quad (5)$$

where A is the absorbance of the material.

The Faradaic efficiency (FE%) of the photoelectrodes is determined by measuring the evolved oxygen gas using the gas chromatography measurements and using the following eq 6

$$\text{FE}\ (\%) = Q_{(O2)}/Q_{(total)} \quad (6)$$

where $Q_{(O2)}$ is the charge equivalent to the evolved oxygen, which is determined from the measured O_2 concentration in moles from the GC measurements and converting it to charge considering the number of holes transferred as 4,[47,48] and $Q_{(total)}$ is the total charge passed in the PEC cell at an applied potential of 1.0 V (RHE) for 1800 s.

Mott−Schottky experiments were performed at 100 Hz in the potential range of −0.54−1.44 V vs RHE to determine the donor density (N_d) and flat band potential (V_{fb}). For the determination of N_d and V_{fb},$1/C^2$ is calculated from impedance and then plotting $1/C^2$ vs applied voltage, and N_d and V_{fb} values are extracted from slope and x axis intercept using the following equation

$$\frac{1}{C^2} = \frac{2}{qA^2\varepsilon\varepsilon_0 N_D}\left(V - V_{FB} - \frac{k_B T}{q}\right) \quad (7)$$

where C is the space charge capacitance, q is the elementary charge, A is the electrode surface area, ε_0 is the vacuum permittivity (8.854 × 10^{-12} F m^{-1}), ε is the relative permittivity of $BiVO_4$ (86), N_D (cm^{-3}) is the donor density, V is the applied potential, V_{FB} is the flat band potential, k_B is the Boltzmann constant (1.38 × 10^{-23} J K^{-1}), and T is the absolute temperature.

Electrochemical impedance spectroscopy (EIS) was recorded at open-circuit potential in the frequency range from 10^5 to 10^{-1} Hz by applying a sinusoidal wave of amplitude 10 mV in both illuminated and dark conditions. Furthermore, EIS data, specifically the Nyquist plot, were fitted into the equivalent circuit model to find out relaxation frequency and time constant of the electron and hole recombination, which indirectly correlates to the efficiency of photoanode materials.

3. RESULTS AND DISCUSSION

3.1. Material Characterization. *3.1.1. XRD Measurements.* The XRD peaks at 26.37 34.58, 37.45, 61.37, and 65.45 show underneath the ITO (JCPDS card 41-1445) substrate. XRD peaks at 2θ values of 18.46, 28.48, 30.10, and 34.95° correspond to the (011), (121), (040), and (002) planes of monoclinic $BiVO_4$ (JCPDS 014-0688), respectively (Figure 1). Upon incorporation of 3D-G, a weak peak around 25 appears, indicating the presence of 3D-G. The $BiVO_4$ phase is preserved after introduction of Co−B_i into the system as no change is observed in peak positions. The XRD plots indicated that the crystallinity of the ITO/SnO_2/3D-G-$BiVO_4$/Co−B_i sample is relatively lower compared to those of the other three samples.

3.1.2. Morphological Characterization. The morphology of the prepared photoanodes was investigated using field emission gun scanning electron microscopy (FEGSEM) and

https://doi.org/10.1021/acsomega.3c03229
ACS Omega 2023, 8, 33452−33465

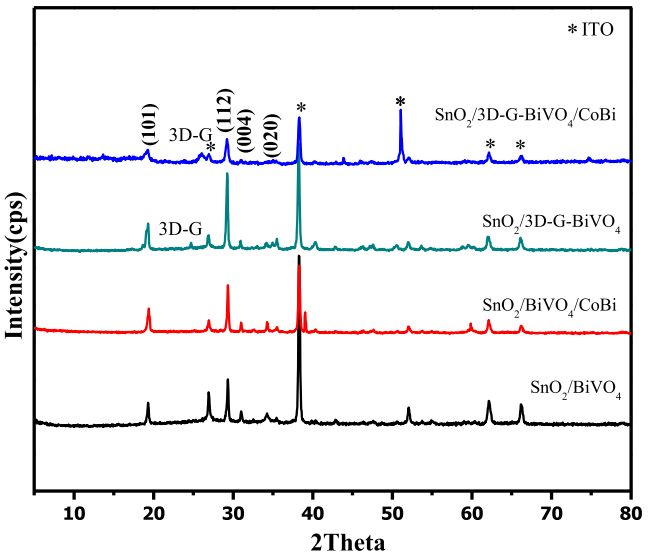

Figure 1. XRD pattern of $SnO_2/BiVO_4$ (black), $SnO_2/BiVO_4/Co{-}B_i$ (red), $SnO_2/3D\text{-}G\text{-}BiVO_4$ (green), and $SnO_2/3D\text{-}G\text{-}BiVO_4/Co{-}B_i$ (blue).

AFM. From SEM images (cf. Figure 2A,B), the granular morphology of the $SnO_2/BiVO_4$ is indicated. On 3D-G incorporation, the overall granular morphology of $BiVO_4$ remained unaltered (Figure 2E,F). Furthermore, uniform deposition of $Co{-}B_i$ over the $SnO_2/BiVO_4$ as well as over $SnO_2/3D\text{-}G\text{-}BiVO_4$ is confirmed from the SEM images (Figure 2C,D,G,H). The AFM investigations are also carried out, and the results are shown in Figure S1 of the Supporting Information. Surface morphologies revealed by AFM investigation corroborate the results obtained by SEM, and the overall granular morphology could be visible from the AFM images. Formation of the $Co{-}B_i$ films could be visible from the covering of the surfaces.

3.1.3. Raman Spectroscopic Measurements. From Raman spectra, the bonding states as coordination polyhedra can be deduced, making it an appropriate technique to study the local structure of the material. In Raman scattering, the characteristics bands of $BiVO_4$ appeared at 333, 365, 710, and 830 cm^{-1}, of which bands at 333 and 365 cm^{-1} can be attributed to asymmetric δ_{as} (VO_4) (A_g) and symmetric δ_s (VO_4) (B_g) deformation modes of VO_4^{3-}, respectively, while bands at 710 and 830 cm^{-1} can be attributed to the symmetric stretching mode of two different types of the V−O bond ν_s (V−O) (A_g).[49] The low intensity of the 710 cm^{-1} band is due to the thin film structure (Figure 3A).[50−53]

Incorporation of 3D-G resulted in an additional band at 1590 cm^{-1}, which is a well-known characteristic of graphene. Additional bands at 475 and 516 cm^{-1} appearing in both $ITO/SnO_2/BiVO_4/Co{-}B_i$ and $ITO/SnO_2/3D\text{-}G\text{-}BiVO_4/Co{-}B_i$ show the mixed phase presence of $Co{-}B_i$ and Co_3O_4, respectively. The overlap of asymmetric δ_{as} (VO_4) (A_g) and symmetric δ_s (VO_4) (B_g) deformation bands and red shift of symmetric ν_s (V−O) (A_g) stretching band from 830 to 813 cm^{-1} indicate deviation toward mesoporous from crystalline structure[54] and quantum confinement effect due to nanoscale grain size of the material.[55−57]

3.1.4. UV−Vis Spectral Measurements. The determination of the band gap of semiconductors is required to predict the photophysical and photochemical properties. The band gap of the material is determined using the Tauc equation as given below

$$(\alpha h\nu)^n = A(h\nu - E_g) \tag{8}$$

where α is the optical absorption coefficient, $h\nu$ is the photon energy, E_g is the band gap, and A is a probability constant. The numerical values of n are $^1/_2$ and 2 for indirect and direct transitions, respectively. Also, the nature of the electronic transition can be found out by from the linearity of $(\alpha h\nu)^n$ vs $h\nu$. If $n = 2$, it is direct allowed transition, or if $n = {}^1/_2$, it is indirect allowed transition. The Tauc plot of the presently investigated materials is shown in Figure 3B,C. All the photoanodes absorb strongly in the range of 330−500 nm, showing broad absorption in the UV−visible range of the solar spectrum. The transition in $BiVO_4$ has been argued with both direct and indirect electronic transitions; in our investigation, we have analyzed the results considering both direct and indirect band gaps, and the corresponding values are tabulated in Table S1 of the Supporting Information.[58−62]

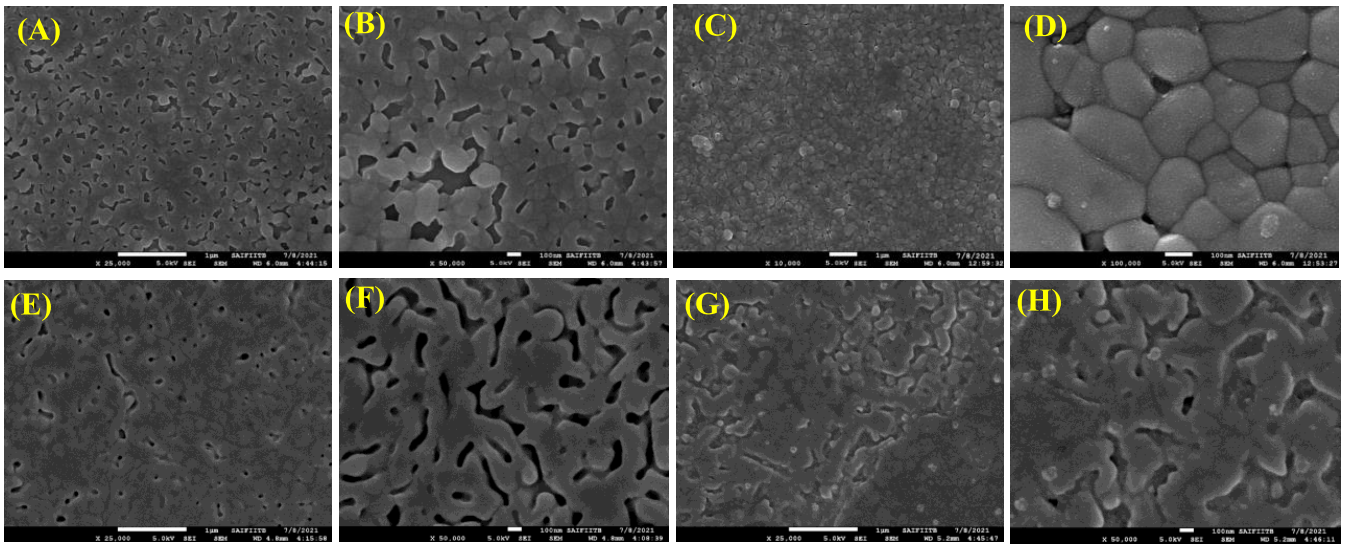

Figure 2. SEM images of (A, B) $SnO_2/BiVO_4$, (C, D) $SnO_2/BiVO_4/Co{-}B_i$, (E, F) $SnO_2/3D\text{-}G\text{-}BiVO_4$, and (G, H) $SnO_2/3D\text{-}G\text{-}BiVO_4/Co{-}B_i$.

https://doi.org/10.1021/acsomega.3c03229
ACS Omega 2023, 8, 33452−33465

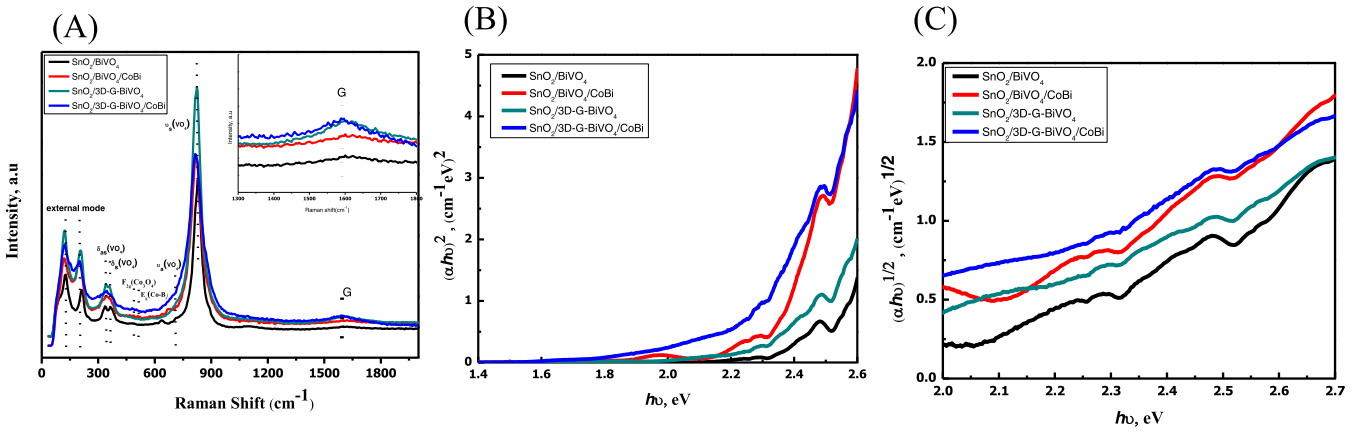

Figure 3. (A) Raman Spectra of $SnO_2/BiVO_4$ (black), $SnO_2/BiVO_4/Co{-}B_i$ (red), SnO_2/3D-G-$BiVO_4$ (green), and SnO_2/3D-G-$BiVO_4/Co{-}B_i$ (blue). (B) Tauc Plot for the direct band gap of $SnO_2/BiVO_4$ (black), $SnO_2/BiVO_4/Co{-}B_i$ (red), SnO_2/3D-G-$BiVO_4$ (green), and SnO_2/3D-G-$BiVO_4/Co{-}B_i$ (blue). (C) Tauc Plot for the direct band gap of $SnO_2/BiVO_4$ (black), $SnO_2/BiVO_4/Co{-}B_i$ (red), SnO_2/3D-G-$BiVO_4$ (green), and SnO_2/3D-G-$BiVO_4/Co{-}B_i$ (blue).

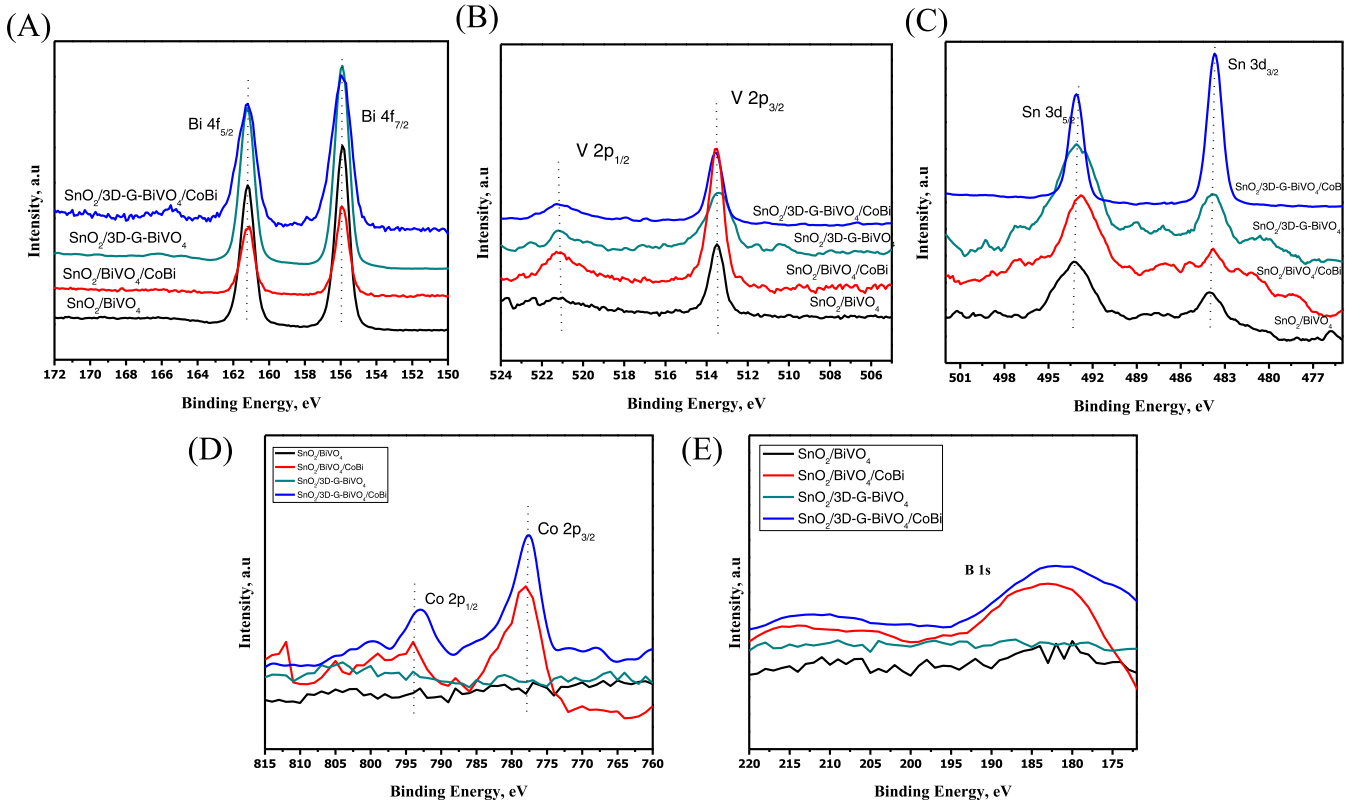

Figure 4. XPS of (A) Bi 4f, (B) V 2p, (C) Sn 3d, (D) Co 2p, and (E) B 1s of $SnO_2/BiVO_4$ (black), $SnO_2/BiVO_4/Co{-}B_i$ (red), SnO_2/3D-G-$BiVO_4$ (green), and SnO_2/3D-G-$BiVO_4/Co{-}B_i$ (blue).

It has been observed that the band gaps calculated considering indirect bands of $BiVO_4$ have been marginally lowered compared to that in the direct one. With incorporation of 3D-G and Co−Bi, the band gaps undergo a downward shift, thus making the threshold wavelength of the absorption shift toward higher wavelength, creating a greater part of the solar spectrum available for absorption compared to pristine $BiVO_4$.

3.1.5. XPS Measurements. Surface chemical states of the photoanodes were investigated by XPS. The measurement provides conclusive evidence of the presence of Bi, V, and O in pristine $BiVO_4$ and the presence of C in 3D-G-incorporated photoanodes and Co in the photoanodes deposited with Co−B_i. From the chemical shift and spin−orbit coupling, split oxidation of the elements can be deduced. The presence of Bi^{3+} is indicated by the peaks due to Bi $4f_{7/2}$ and Bi $4f_{5/2}$ at 155.9 and 161.26 eV with doublet energy splitting at 5.36 eV (Figure 4A) and peaks at 516.52 and 524.14 eV with spin−orbit split of 7.62 eV indicates V^{5+} (Figure 4B). The presence of Co^{3+} is confirmed from the peaks at 780.30 and 795.27 eV, which are due to Co $2p_{3/2}$ and Co $2p_{1/2}$ (Figure 4C,D), respectively. The peak at 187 eV is a well-known signature of the B 1s orbital, indicating the presence of boron (Figure 4E). The presence of oxygen is inferred from the O 1s cumulative

https://doi.org/10.1021/acsomega.3c03229
ACS Omega 2023, 8, 33452−33465

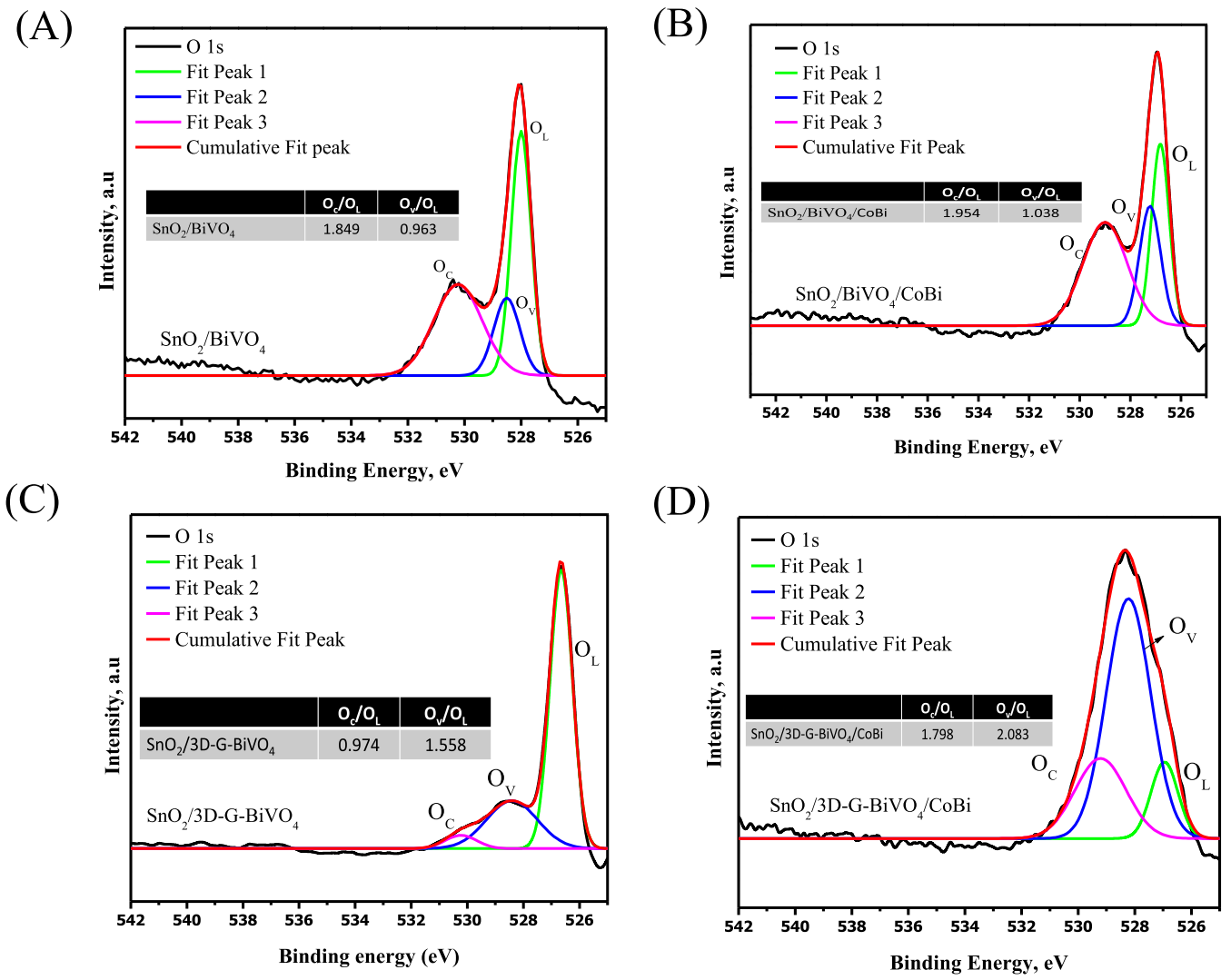

Figure 5. XPS of O 1s of (A) $SnO_2/BiVO_4$, (B) $SnO_2/BiVO_4/Co{-}B_i$, (C) SnO_2/3D-G-$BiVO_4$, and (D) SnO_2/3D-$BiVO_4/Co{-}B_i$.

asymmetric peaks at binding energies of 533 and 531 eV. These peaks can be deconvoluted into peaks with binding energies of 529.9, 530.5, and 532.3 eV, which are attributed to O^{2-} at the lattice site (O_L), vacancy region (Ov),[63] and chemisorbed oxygen (Oc) and water, respectively.[64] Oxygen vacancy is known to improve the catalytic activity of the $BiVO_4$ photoanode.[21,22] From the Ov/O_L ratios, it can be observed that the ratio is almost similar (~0.97) in the case of $SnO_2/BiVO_4$ and 1.04 in $SnO_2/BiVO_4/Co{-}B_i$, while with incorporation of 3D-G, it increases the Ov/O_L ratio to 1.56 in SnO_2/3D-G-$BiVO_4$ and 2.08 in SnO_2/3D-G-$BiVO_4/Co{-}B_i$ (Figure 5). The inclusion of Co has an influence in enhancement in the oxygen vacancy, which has been reflected in the present measurement, where in the $Co{-}B_i$-containing samples, the Ov/O_L ratio has been increased.[65] However, the majority of the enhancement in the oxygen vacancy has been created by the inclusion of 3D-G. The oxygen vacancy has always played an active role in the enhancement of PEC efficiency, and it would therefore be interesting in the present case as well to observe its influence. There are arguments about the measurement of oxygen vacancies from the XPS techniques.[66] Samples are kept inside a desiccator to avoid any adsorption of oxygen from the atmosphere during the transfer of samples from its synthesis to the XPS measurement facility. The kinetic energy of electrons coming out from the oxygen with stoichiometry fulfilled and unfulfilled and the chemisorbed oxygen are bound to be different; therefore, the argument of observation of peaks of O_L, Ov, and Oc and measurement of their relative presence from XPS could be used in comparing the performance across samples of the same series.[67]

3.2. Photoelectrochemical Investigation. Photoelectrochemical investigations have been carried out for all the photoanodes under AM 1.5 G-simulated illumination using a xenon lamp. The 0.5 M Na_2SO_4 in borate buffer of pH 8 has been used as the electrolyte, instead of using phosphate buffer due to its corrosive nature for $BiVO_4$ systems.[13] The performance of the photoanodes was investigated by LSV and chopped light voltammetry (CLV), and the results are shown in Figure 6A,B. Current densities obtained at 1.19 V vs RHE for $SnO_2/BiVO_4$, SnO_2/3D-G $BiVO_4$, $SnO_2/BiVO_4/Co{-}B_i$, and SnO_2/3D-G-$BiVO_4/Co{-}B_i$ are 0.74, 0.90, 1.23, and 1.48 mA cm^{-2}, respectively. The enhancement in PEC current with the incorporation of 3D-G is ~165%, signifying the definite and quantitative role of 3D-G in enhancing the photocurrent density of the electrodes. Moreover, 3D-G-incorporated photoanodes show high current density even at a lower applied bias. The enhancement in the current density on 3D-G incorporation is more prominent at the lower applied

https://doi.org/10.1021/acsomega.3c03229
ACS Omega 2023, 8, 33452−33465

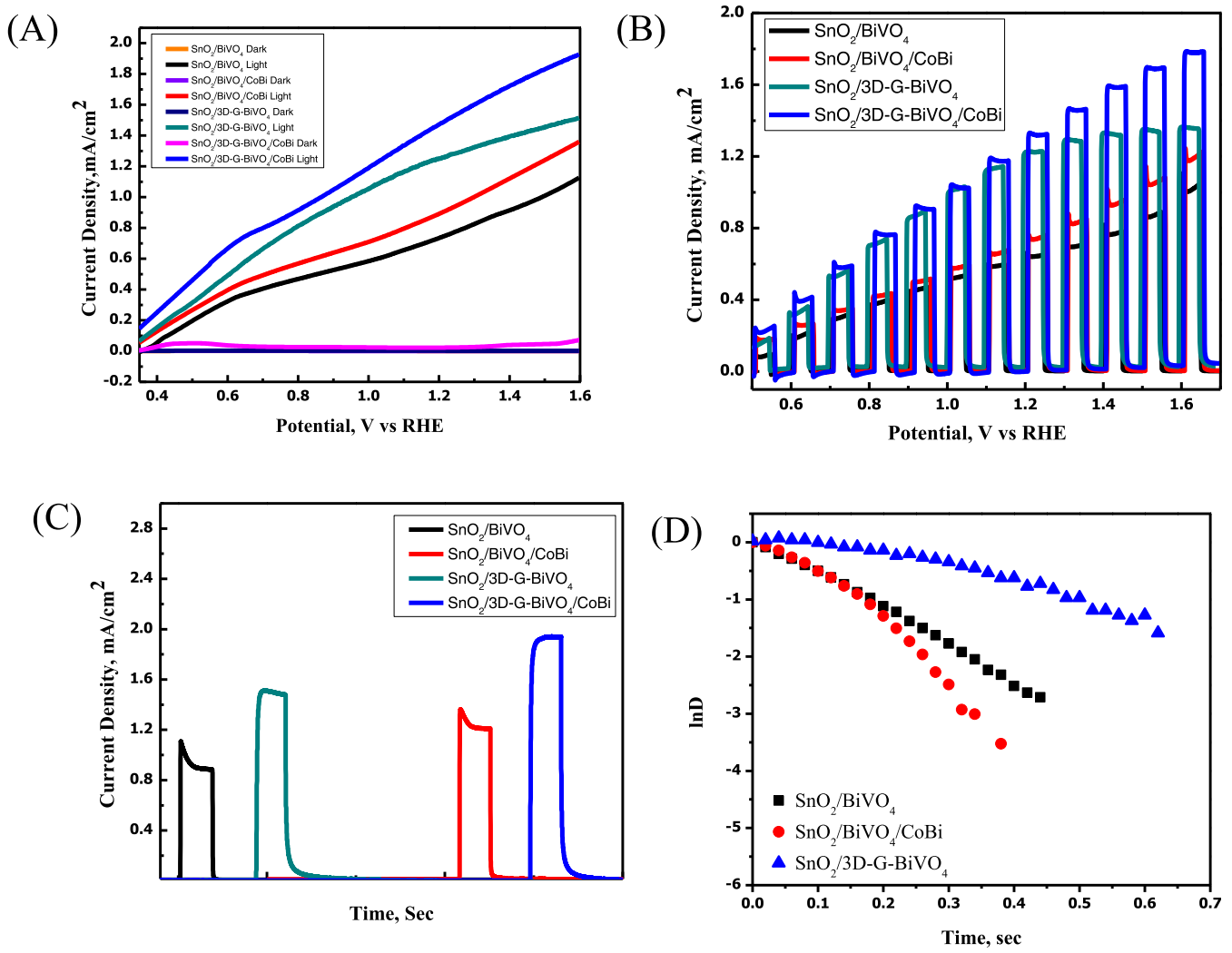

Figure 6. (A) Linear sweep voltammetry (BBS Buffer pH 8) and (B) chopped light voltammetry for $SnO_2/BiVO_4$ (black), $SnO_2/BiVO_4/Co{-}B_i$ (red), SnO_2/3D-G-$BiVO_4$ (green), and SnO_2/3D-G-$BiVO_4/Co{-}B_i$ (blue). (C) Transient study for $SnO_2/BiVO_4$ (black), $SnO_2/BiVO_4/Co{-}B_i$ (red), SnO_2/3D-G-$BiVO_4$ (green), and SnO_2/3D-G-$BiVO_4/Co{-}B_i$ (blue). (D) ln *D* vs time graph for $SnO_2/BiVO_4$ (black), $SnO_2/BiVO_4/Co{-}B_i$ (red), and SnO_2/3D-G-$BiVO_4$ (blue).

potential. The shape of the LSV plot is different in the case of 3D-G-containing samples compared to the samples with the absence of 3D-G.[11,68] The presence of 3D-G has improved the conductivity, which has enhanced the photocurrent at lower overpotential. For the samples without 3D-G, the photocurrent remained lower at lower bias potential; however, when the bias potential (1.3 V vs RHE) is sufficient to drive the majority of the carrier back to the sink, the current picked up very fast afterward.

The chopped light voltammetry experiments were carried out, and the results are shown in Figure 6B. A similar trend as that for linear sweep voltammetry can be observed in the current density of all the catalyst materials. Just after the light-off stage, a reduction in current has been observed in samples where 3D-G is not present. With an increase in overpotential, the reduction current disappears. The absence of the reduction current in SnO_2/3D-G-$BiVO_4$ even at lower overpotential than that of $SnO_2/BiVO_4$ indicates the efficient transfer of electrons toward the sink and effective separation of the e−h pair by the enhanced conductivity of 3D-G. It may also be noted that the reduction current is more prominent after the introduction of $Co{-}B_i$ in the system, which essentially explains the basic idea of introducing $Co{-}B_i$ to enhance the interfacial transfer of holes toward the solution. Therefore, immediately after turning the illumination off, the electrons would remain in excess for the Co−Bi-containing samples without 3D-G, and the excess electrons would result in minor reduction current after the illumination is turned off. Such reduction current is not observed with the introduction of 3D-G into the $Co{-}B_i$-containing system, as 3D-G would help in transfer of electrons toward the sink.

The transient nature of the photocurrent across all the materials is recorded and shown in Figure 6C. As the photoelectrode is illuminated, an initial spike is observed due to the immediate separation of the e−h pair. Electrons move toward ITO, while holes move toward the electrolyte interface to oxidize water. Additionally, the holes react with conduction band electrons and undergo recombination. The decay in the initial photocurrent has been observed with the $SnO_2/BiVO_4$ and $SnO_2/BiVO_4/Co{-}B_i$ photoanodes, whereas the decay has been less significant with the SnO_2/3D-G-$BiVO_4$ and SnO_2/3D-G-$BiVO_4/Co{-}B_i$ photoanodes. In order to obtain the decay profile of the photocurrent, the transient photocurrent is fitted using the following dimensionless parameter *D*

https://doi.org/10.1021/acsomega.3c03229
ACS Omega 2023, 8, 33452−33465

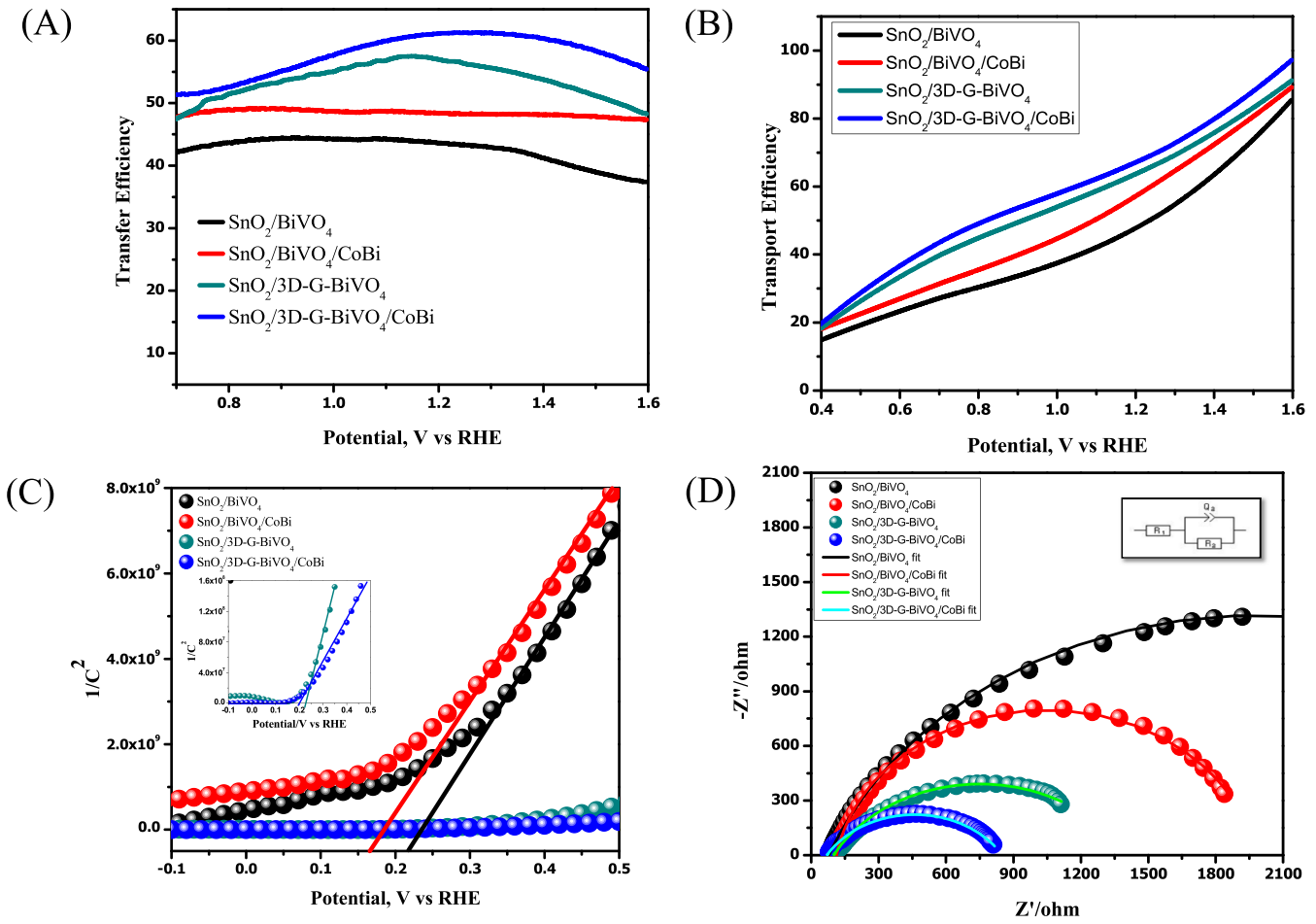

Figure 7. (A) Transfer efficiency. (B) Transport Efficiency. (C) Mott−Schottky Plot at 100 Hz. (D) Nyquist Plot of $SnO_2/BiVO_4$ (black), $SnO_2/BiVO_4$/Co−B_i (red), SnO_2/3D-G-$BiVO_4$ (green), and SnO_2/3D-G-$BiVO_4$/Co−B_i (blue).

$$D = (I_{(t)} - I_{(st)})/(I_{(in)} - I_{(st)}) \quad (9)$$

where $I_{(t)}$ is the photocurrent at time t, $I_{(in)}$ is the initial photocurrent measured at $t = 0$, and $I_{(st)}$ is the steady photocurrent. The transient time constant (τ) is defined as the time at which $\ln(D) = -1$.[69] The transient behavior of the photoanodes has been studied by illuminating the photoanodes for a short time period of 1 s at 1.19 V vs RHE, and the decay characteristic is observed (Figure 6D). The value of the observed τ is 0.17 0.19, and 0.5 s for $SnO_2/BiVO_4$, $SnO_2/BiVO_4$/Co−B_i, and SnO_2/3D-G-$BiVO_4$ samples, respectively, while SnO_2/3D-G-$BiVO_4$/Co−B_i does not show any significant decay. Photoelectrochemical efficiency of $BiVO_4$ remains low due to the fast charge recombination due to numerous recombination and charge trapping centers. Incorporation of 3D-G provides low-energy pathways for the photogenerated charges due to high electronic conductivity, thereby reducing the recombination as reflected by the transient time constant. Lower recombination is the reason behind the enhanced photocurrent density.

3.3. Efficiency Measurements and Mott−Schottky Analysis. To further understand the photoelectrochemical properties of the fabricated photoanodes, the IPCE was calculated. Correlation between the efficiency and wavelength is extracted from IPCE measurements and plotted in Figure S2 of the Supporting Information. IPCE of $SnO_2/BiVO_4$ is ∼20%, while the efficiency of SnO_2/3D-G-$BiVO_4$, $SnO_2/BiVO_4$/Co−B_i, and SnO_2/3D-G-$BiVO_4$/Co−B_i is ∼27, 23, and 32%, respectively.[70,71] The photocurrent density plots of the photoanodes at different wavelengths are included in Figure S3 of the Supporting Information.

The APCE has also been measured, and the values are plotted in Figure S4 of the Supporting Information. As expected, the APCE results follow the same trend as that of IPCE. APCE increases as the applied bias increases due to efficient e−h separation. APCE increases for $SnO_2/BiVO_4$ as higher potential is applied. (Figure S4) A similar pattern is seen in the case of $SnO_2/BiVO_4$/Co−B_i, while in the case of SnO_2/3D-G-$BiVO_4$, enhancement in current is observed due to effective separation of photogenerated charge carriers even at lower applied potential. As Co−B_i is introduced, APCE of SnO_2/3D-G-$BiVO_4$/Co−B_i again increases with an increase in applied bias as new redox centers are available and activity of the cocatalyst increases with the applied bias. The FE (%) for the samples $SnO_2/BiVO_4$, SnO_2/3D-G $BiVO_4$, $SnO_2/BiVO_4$/Co−B_i, and SnO_2/3D-G-$BiVO_4$/Co−B_i is 87, 86, 90, and 89, respectively. The results thus indicate the insignificant contribution of the non-Faradaic processes in the overall current during PEC oxidation of water.[47,48,72]

The photoelectrochemical investigations carried out so far have indicated that the photocurrent undergoes enhancement on the incorporation of 3D-G in $BiVO_4$, which has been evidenced from the LSV and CLV measurements. The current transient behaviors have indicated the enhancement of lifetime

https://doi.org/10.1021/acsomega.3c03229
ACS Omega 2023, 8, 33452−33465

Table 1. Parameters Obtained from the Mott−Schottky and Electrochemical Impedance Measurements

photoelectrode	R_{sol} (Ω)	Q_1	n	R_{ct} (Ω)	C (μF)	relaxation frequency (Hz)	relaxation time constant (ms)	L_D (hole diffusion length) (μm)	donor density	flat band potential (V) vs RHE
$SnO_2/BiVO_4$	80	15×10^{-6}	0.77	3890	6.42	60	2.65	117	5.64×10^{20}	0.205
$SnO_2/BiVO_4/Co-B_i$	100	30×10^{-6}	0.90	1890	21.81	380	0.42	47	7.93×10^{20}	0.146
SnO_2/3D-G-$BiVO_4$	100.8	70×10^{-6}	0.689	1300	23.73	40	3.98	144	3.23×10^{22}	0.233
SnO_2/3D-G-$BiVO_4/Co-B_i$	70	140×10^{-6}	0.66	780	44.74	90	1.77	96	3.84×10^{22}	0.207

of the charge carriers. The quantification of improvement of performance to the surface charge recombination and the bulk charge recombination has been evaluated from the measurements of the surface charge separation ($\eta_{transfer}$) and bulk charge separation ($\eta_{transport}$) efficiencies of the photoanodes using the procedures as explained in eqs 1, 2, and 3 in the experimental section. The results are plotted in Figure 7A,B. The $\eta_{transfer}$ has been improved upon inclusion of Co−B_i in the $BiVO_4$ sample due to the electrocatalytic activity and efficient transfer of surface charges to the solution. The presence of 3D-G has significant enhancement in the surface charge separation process, which indicates that 3D-G has a positive role in the enhancement of surface conductivity of the material, which resulted in the efficient transfer of holes to the solution. The variation of $\eta_{transport}$ with respect to the applied bias potentials is also plotted and shown in Figure 7B. The significant enhancement of the ($\eta_{trasport}$) especially at the lower overpotentials upon incorporation of 3D-G has clear indication about the improvements in e−h recombination of the materials.

The effective enhancement in charge carrier generation and their separation can be derived from Mott−Schottky analysis. As it involves impedance over a range of potentials, it represents convolution of transport and transfer of charges. As the electrode−electrolyte comes in contact, transfer of electrons from the conduction band of the electrode to the suitable redox centers in the electrolyte occurs to maintain both the Fermi levels at the same energy, leading to band bending. The larger the band bending, the better the charge separation. The electron leaves the electrode, thereby generating the space charge layer. Space charge capacitance depends upon many factors as shown in eq 6, from which the flat band potential and interfacial donor density can be extracted. Figure 7C shows the Mott−Schottky plot of the photoanodes recorded under illumination conditions using a solar simulator. Donor density and flat band potential calculated from the Mott−Schottky plot are tabulated in Table 1. For $SnO_2/BiVO_4$, the donor density was obtained as 5.64×10^{20}, while there is a slight increase in donor density with incorporation of Co−B_i. Introduction of 3D-G enhances the donor density by 1 order of magnitude, which is indicative of the presence of a large number of charge carriers because of lesser recombination owing to the high conductivity. Improvement in e−h separation is also indicated from the flat band potential. It increases from 0.205 in SnO_2−$BiVO_4$ to 0.233 in SnO_2/3D-G-$BiVO_4$, indicating greater band bending, which facilitates better charge separation. The incorporation of Co−B_i has resulted in cathodic shifting of the flat band potentials without decreasing in the donor density in both the $SnO_2/BiVO_4/Co-B_i$ and SnO_2/3D-G-$BiVO_4/Co-B_i$ samples. Cathodic shift in the flat band potential indicates a lower onset potential, which can be corroborated from the LSV plot.

The frequency-dependent behavior of the system is measured in terms of complex current under perturbed potential. The resulted Nyquist plots are shown in Figure 7D. The obtained data were suitably modeled using Randle's circuit, and the evaluated parameters are placed in Table 1.[73] Charge transfer resistance decreases steadily from $SnO_2/BiVO_4$ to SnO_2/3D-G-$BiVO_4$ with the inclusion of 3D-G in the sample. The lowest charge transfer resistance has been observed in the case of SnO_2/3D-G-$BiVO_4/Co-B_i$, indicating better charge transfer and performance. The evaluation of R_{ct} from the impedance measurement is consistent with the photocurrent obtained with the electrodes tested using LSV, CLV, and Mott−Schottky studies. The depressed semicircle indicates the nonideal capacitive nature of the electrode, resulting from the inhomogeneous electrochemical processes from the entire substrate; the degree of inhomogeneity is numerically related with the n factor. Inclusion of 3D-G in the photoanode has resulted in a lower n factor, indicated with more surface roughness. Inclusion of 3D-G has improved the capacitance of $SnO_2/BiVO_4$ from 6.42 to 23.73 μF in the SnO_2/3D-G-$BiVO_4$ sample. Similar improvement was observed for $SnO_2/BiVO_4/Co-B_i$ and SnO_2/3D-G-$BiVO_4/Co-B_i$.

The improvement in capacitance is closely linked to the surface charge density of the photoanodes, which has been improved due to the inclusion of 3D-G in the sample; the enhancement of surface charge density due to the incorporation of Co−B_i has been in the line with our previous publications.[40] For a relative comparison of interfacial kinetics, the relaxation process of the photoanodes was evaluated by sampling the frequency maxima of the Bode plot. Maxima of the Bode plot correspond to the relaxation frequency (f). The relaxation time constant (τ) was further calculated using $\tau = 1/2\pi f$. The values are tabulated in Table 1, and the relaxation frequency was found to be in the order of hundreds of Hz, while the relaxation time constant for the electrochemical process was on the order of milliseconds for all the samples. The inclusion of Co−B_i has decreased the relaxation time constant through enhancement in the charge transfer process through improvements in the surface hole transfer kinetics, whereas the inclusion of 3D-G has enhanced the relaxation time constant. Interestingly, the inclusion of both 3D-G and Co−B_i with $BiVO_4$ has increased the photocurrent.

The diffusion length (L_D) of the minority carrier, i.e., photogenerated holes, is calculated from the relaxation time constant and diffusion coefficient for the holes using the relation $L_D = (D \times \tau)^{1/2}$, where L_D is the diffusion length and D is the diffusion coefficient of the photogenerated hole, taken as 5.2×10^{-2} cm^2 s^{-1}. Diffusion length is a very important parameter for interfacial charge transfer reactions. Hole diffusion length for $SnO_2/BiVO_4$ is 117 μm, whereas for $SnO_2/BiVO_4/Co-B_i$, it is 47 μm, and it increases with 3D-G incorporation to 144 μm, and for SnO_2/3D-G-$BiVO_4/Co-B_i$,

https://doi.org/10.1021/acsomega.3c03229
ACS Omega 2023, 8, 33452−33465

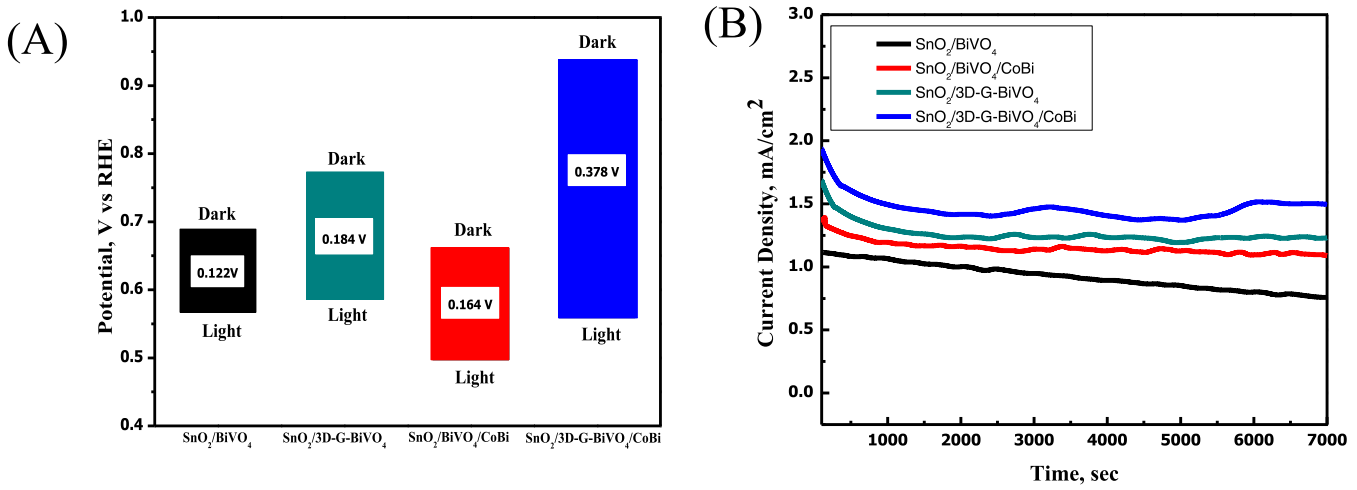

Figure 8. (A) Open-circuit potential of $SnO_2/BiVO_4$ (black), $SnO_2/BiVO_4/Co{-}B_i$ (red), SnO_2/3D-G-$BiVO_4$ (green), and SnO_2/3D-G-$BiVO_4$/$Co{-}B_i$ (blue). (B) Stability test for $SnO_2/BiVO_4$ (black), $SnO_2/BiVO_4/Co{-}B_i$ (red), SnO_2/3D-G-$BiVO_4$ (green), and SnO_2/3D-G-$BiVO_4$/$Co{-}B_i$ (blue).

Scheme 1. Schematic Representation of the Energy Level Diagram of the Fermi levels, Quasi-Fermi levels, and the Redox Levels of the Semiconductor and Liquid Interface

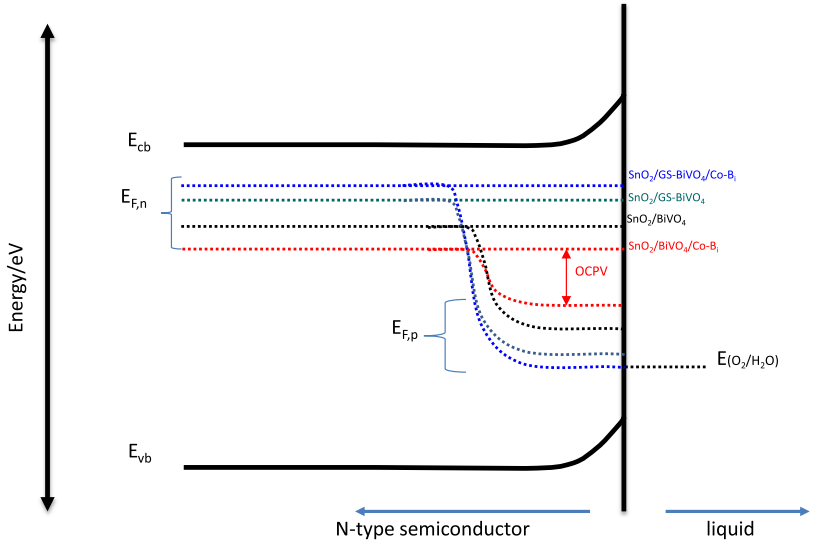

it again decreases to 96 μm. The comparison of the diffusion length values among all the photoelectrodes thus indicates that inclusion of 3D-G has enhanced the diffusion length, further supporting the fact that the electron and hole recombination process is decreased and holes can be transported from deeper inside the photoelectrode containing 3D-G to the interface. Since $Co{-}B_i$ has improved the surface charge transfer step, the hole transfer kinetics is enhanced, which has resulted in the decrease in the relaxation time, and thus, the diffusion length seems to have been reduced. The relaxation time measured using the time-resolved spectroscopic measurements considers the time for its de-excitation process, whereas the hole takes some more time for its complete relaxation/interfacial process. EIS measurements are capable of proving the categorized information about the relaxation processes inside the solid electrode and at the interface; presently, the EIS data have been fitted with a simple Randle circuit, where the resulting relaxation time includes all the process involved at the photoelectrode.[58,74−81] The diffusion length measured from the spectroscopic technique varies in a few nanometer range, whereas the diffusion length values reported from the Bode plots fall over 100 μm. The lifetime measurements from the time-resolved spectroscopic technique consider the lifetime of the holes at the excited state, which are related to the electronic structure and electronic conductivity. It is important to further emphasize that the diffusion length calculated using the relaxation time utilizes the relaxation of all the processes together, which is under the assumption that the relaxation time constant includes both the time taken by the photogenerated charge carrier in the bulk, i.e., from bulk to the interface as well as at the electrode/electrolyte interface, i.e., from the interface to the electrolyte where it oxidizes water molecules. Incorporation of 3D-G enhances the lifetime of holes by reducing the possibility of electron−hole recombination and incorporation of $Co{-}B_i$ essentially decreases the lifetime of the hole through its efficient transfer to the solution; therefore, both the processes have a contradicting effect on the value of the relaxation time; however, both of them eventually lead to the enhancement in the PEC current. The investigations from the electrochemical impedance spectros-

https://doi.org/10.1021/acsomega.3c03229
ACS Omega 2023, 8, 33452−33465

copy, therefore, support the interesting roles of 3D-G and Co−B_i in improving the charge transfer kinetics, resulting in the enhancement of photocurrent.

3.4. Open-Circuit Photovoltage (OCPV) and Stability of the Photoanodes. The concentrations of the interfacial charge carrier and the energetics of the charge carriers are important in determining the PEC water splitting efficiency. Under dark conditions, the $BiVO_4$ being an n-type semiconductor has excess positive charge over the depletion region inside the semiconductor, while the negative dipoles are concentrated along the Helmholtz layer, while the semiconductor electrode is placed in solution.[82] The extent of the band bending depends on the difference between the initial Fermi level of the semiconductor and the redox potential of $E°(O_2/H_2O)$. The difference of energy essentially directs the holes toward the electrolyte solution.[83−87] On illumination, the open-circuit potential (OCP) undergoes negative shifting in all of the samples. Inclusion of 3D-G has an effect on the release of the Fermi level pinning, and the OCP in the dark has a positive shifting. The open-circuit photovoltage (OCPV), measured from the difference in the OCP in the dark to that under illumination, has been significantly enhanced with the incorporation of 3D-G into the samples. Hence, the more the OCPV, the more effective the electron−hole separation. The quasi-Fermi level splitting increases from 0.122 V (SnO_2/$BiVO_4$) to 0.184 V(SnO_2/3D-G-$BiVO_4$), the highest being 0.378 V in the case of SnO_2/3D-G-$BiVO_4$/Co−B_i (Figure 8A).[88]

The relaxation of the Fermi level pinning effect on inclusion of 3D-G has associated kinetics, resulting in higher catalytic performances. With inclusion of 3D-G, the conductivity of the material has been improved, which has been reflected from the shifting of open-circuit potential even in dark conditions, resulting in the closeness of the Fermi level to the CB of the semiconductor. Upon illumination, the quasi-Fermi level hole $E_{F,p}$ at interface is lowered down. The scenario is qualitatively represented in Scheme 1. The highest shifting in the $E_{F,p}$ is depicted in the case of SnO_2/3D-G-$BiVO_4$/Co−B_i, which has shown the highest OCPV value upon illumination. The lowering of the $E_{F,p}$ due to the inclusion of 3D-G has impacted better band alignment with the solution side and thus resulted in enhancement in the catalytic preferences of the photoanodes. As has been observed from the XRD measurements, the crystallinity of the ITO/SnO_2/3D-G-$BiVO_4$/Co−B_i sample is relatively lower. Improvement of the PEC catalytic performance has been reported in $BiVO_4$, while the better crystalline materials were obtained through increasing the annealing temperature.[68,76] Therefore, the sample with the chemical composition SnO_2/3D-G-$BiVO_4$/CoB_i with better crystallinity has further scope of improvement in the catalytic performance as the photoanode.

After having a discussion about the improvement in the catalytic performances on inclusion of 3D-G in the $BiVO_4$ matrix, it is important to carry out the measurement of the stability of the electrodes on prolonged light exposures. Although $BiVO_4$ is known for its stability in near-neutral pH solutions, under illumination, the anodic shift of the quasi-Fermi level of holes triggers additional anodic reactions along with the OER, leading to light-driven corrosion of $BiVO_4$.[89−91] Photostability of the prepared photoanodes is demonstrated by stable chronoamperometric curves shown in Figure 8B. Among all the four modified electrodes tested, the bare $BiVO_4$ is the least stable, showing almost 25% reduction of initial photocurrent during the test period, while the rest of the photoanodes maintain stable photocurrent. SnO_2/3D-G-$BiVO_4$/Co−B_i is the most stable among all of the photoanodes investigated. Due to having the least transfer coefficient, bare $BiVO_4$ would have the highest unused holes at the interface, which provides sufficient time to such stagnant holes available for the photocorrosion processes. Photoanodes in which Co−B_i is present act as a relay for the holes between the electrolyte and $BiVO_4$, leaving lesser holes for the photocorrosion reaction. In the presence of 3D-G as well as the Co−B_i, in the SnO_2/3D-G-$BiVO_4$/Co−B_i sample, the 3D-G would enhance the transport of the majority carrier toward the sink and Co−B_i would help in the enhancement of the charge transfer at the interface; thus, the stagnation of holes at the interface does not arise, which essentially reduces the possibility of the photocorrosion process.

4. CONCLUSIONS

The present investigation has focused on the enhancement in the photocatalytic efficiency of $BiVO_4$-based photoanodes for oxidation of water to oxygen. The charge carrier efficiency for both the majority and the minority carrier has been enhanced. The SnO_2 heterojunction has been formed as the conventional way to enhance the removal of the photogenerated majority carrier from the $BiVO_4$ semiconductor. The main motivation has been to introduce the 3D-G with the primary aim in enhancing the conductivity of the photoanode, which eventually resulted in enhancing both the charge transport and the charge transfer efficiencies. The enhancement of the charge transport with 3D-G has reduced the bulk recombination of the photogenerated charge carriers. The lifetime of the charge carrier has been increased. The decrease in the decay kinetics of the holes, enhancement in the OCPV, and the resulting modulation of the surface states are responsible for the enhancement in the surface charge transfer process due to the inclusion of 3D-G into the catalytic system. Therefore, the additional role of 3D-G in the modulation of the surface states and release of the Fermi level pinning has allowed better band alignment between the semiconductor and the analyte in the solution, which resulted in enhanced catalytic performance in the photoelectrochemical oxidation of water.

■ ASSOCIATED CONTENT

Supporting Information

The Supporting Information is available free of charge at https://pubs.acs.org/doi/10.1021/acsomega.3c03229.

Band gaps of the samples and AFM images of the photoanodes and the plots related to the IPCE and APCE measurements (PDF)

■ AUTHOR INFORMATION

Corresponding Author

Ashis Kumar Satpati − *Analytical Chemistry Division, Bhabha Atomic Research Centre, Mumbai 400085, India; Homi Bhabha National Institute, Mumbai 400094, India;* orcid.org/0000-0002-2732-8706; Email: asatpati@barc.gov.in

Authors

Abhishek Sharma − *Analytical Chemistry Division, Bhabha Atomic Research Centre, Mumbai 400085, India; Homi Bhabha National Institute, Mumbai 400094, India*

https://doi.org/10.1021/acsomega.3c03229
ACS Omega 2023, 8, 33452−33465

Sudipa Manna − *Analytical Chemistry Division, Bhabha Atomic Research Centre, Mumbai 400085, India; Homi Bhabha National Institute, Mumbai 400094, India*
Sriram Kumar − *Analytical Chemistry Division, Bhabha Atomic Research Centre, Mumbai 400085, India; Homi Bhabha National Institute, Mumbai 400094, India*

Complete contact information is available at: https://pubs.acs.org/10.1021/acsomega.3c03229

Notes

The authors declare no competing financial interest.

■ ACKNOWLEDGMENTS

The authors thank the Bhabha Atomic Research Centre (BARC) for fully funding the project. A.S. thanks the HBNI for the fellowship. The authors also thank Prof. A. K. Tyagi, Director, Chemistry Group, and Prof. C. N. Patra, Head, Analytical Chemistry Division, for the encouragements and supports in the project.

■ REFERENCES

(1) Hisatomi, T.; Kubota, J.; Domen, K. Recent advances in semiconductors for photocatalytic and photoelectrochemical water splitting. *Chem. Soc. Rev.* **2014**, *43* (22), 7520−7535.
(2) Bhatt, M. D.; Lee, J. S. Recent theoretical progress in the development of photoanode materials for solar water splitting photoelectrochemical cells. *J. Mater. Chem. A* **2015**, *3* (20), 10632−10659.
(3) Kment, S.; Riboni, F.; Pausova, S.; Wang, L.; Wang, L.; Han, H.; Hubicka, Z.; Krysa, J.; Schmuki, P.; Zboril, R. Photoanodes based on TiO 2 and α-Fe 2 O 3 for solar water splitting−superior role of 1D nanoarchitectures and of combined heterostructures. *Chem. Soc. Rev.* **2017**, *46* (12), 3716−3769.
(4) Butburee, T.; Bai, Y.; Wang, H.; Chen, H.; Wang, Z.; Liu, G.; Zou, J.; Khemthong, P.; Lu, G. Q. M.; Wang, L. 2D porous TiO2 single-crystalline nanostructure demonstrating high photo-electrochemical water splitting performance. *Adv. Mater.* **2018**, *30* (21), No. 1705666.
(5) Wang, S.-C.; Tang, F.-Q.; Wang, L.-Z. Visible light responsive metal oxide photoanodes for photoelectrochemical water splitting: a comprehensive review on rational materials design. *J. Inorg. Mater.* **2018**, *33* (2), 173 DOI: 10.15541/jim20170352.
(6) Kumar, S.; Ahirwar, S.; Satpati, A. K. Insight into the PEC and interfacial charge transfer kinetics at the Mo doped BiVO 4 photoanodes. *RSC Adv.* **2019**, *9* (70), 41368−41382.
(7) Kim, T. W.; Choi, K.-S. Nanoporous BiVO4 photoanodes with dual-layer oxygen evolution catalysts for solar water splitting. *Science* **2014**, *343* (6174), 990−994.
(8) Ager, J. W.; Shaner, M. R.; Walczak, K. A.; Sharp, I. D.; Ardo, S. Experimental demonstrations of spontaneous, solar-driven photo-electrochemical water splitting. *Energy Environ. Sci.* **2015**, *8* (10), 2811−2824.
(9) Cho, S. K.; Park, H. S.; Lee, H. C.; Nam, K. M.; Bard, A. J. Metal doping of BiVO4 by composite electrodeposition with improved photoelectrochemical water oxidation. *J. Phys. Chem. C* **2013**, *117* (44), 23048−23056.
(10) Sinclair, T. S.; Hunter, B. M.; Winkler, J. R.; Gray, H. B.; Müller, A. M. Factors affecting bismuth vanadate photoelectrochemical performance. *Mater. Horiz.* **2015**, *2* (3), 330−337.
(11) Seabold, J. A.; Choi, K.-S. Efficient and stable photo-oxidation of water by a bismuth vanadate photoanode coupled with an iron oxyhydroxide oxygen evolution catalyst. *J. Am. Chem. Soc.* **2012**, *134* (4), 2186−2192.
(12) Eisenberg, D.; Ahn, H. S.; Bard, A. J. Enhanced photo-electrochemical water oxidation on bismuth vanadate by electro-deposition of amorphous titanium dioxide. *J. Am. Chem. Soc.* **2014**, *136* (40), 14011−14014.
(13) Toma, F. M.; Cooper, J. K.; Kunzelmann, V.; McDowell, M. T.; Yu, J.; Larson, D. M.; Borys, N. J.; Abelyan, C.; Beeman, J. W.; Yu, K. M.; et al. Mechanistic insights into chemical and photochemical transformations of bismuth vanadate photoanodes. *Nat. Commun.* **2016**, *7* (1), No. 12012.
(14) Yang, J. W.; Park, I. J.; Lee, S. A.; Lee, M. G.; Lee, T. H.; Park, H.; Kim, C.; Park, J.; Moon, J.; Kim, J. Y.; Jang, H. W. Near-complete charge separation in tailored BiVO4-based heterostructure photo-anodes toward artificial leaf. *Appl. Catal., B* **2021**, *293*, No. 120217.
(15) Bhat, S. S. M.; Suh, J. M.; Choi, S.; Hong, S.-P.; Lee, S. A.; Kim, C.; Moon, C. W.; Lee, M. G.; Jang, H. W. Substantially enhanced front illumination photocurrent in porous SnO 2 nanorods/networked BiVO 4 heterojunction photoanodes. *J. Mater. Chem. A* **2018**, *6* (30), 14633−14643.
(16) Zhou, L.; Zhao, C.; Giri, B.; Allen, P.; Xu, X.; Joshi, H.; Fan, Y.; Titova, L. V.; Rao, P. M. High light absorption and charge separation efficiency at low applied voltage from Sb-doped SnO2/BiVO4 core/shell nanorod-array photoanodes. *Nano Lett.* **2016**, *16* (6), 3463−3474.
(17) Byun, S.; Kim, B.; Jeon, S.; Shin, B. Effects of a SnO 2 hole blocking layer in a BiVO 4-based photoanode on photoelectrocatalytic water oxidation. *J. Mater. Chem. A* **2017**, *5* (15), 6905−6913.
(18) Bera, S.; Lee, S. A.; Kim, C.-M.; Khan, H.; Jang, H. W.; Kwon, S.-H. Controlled synthesis of vertically aligned SnO2 nanograss-structured thin films for SnO2/BiVO4 core−shell heterostructures with highly enhanced photoelectrochemical properties. *Chem. Mater.* **2018**, *30* (23), 8501−8509.
(19) Pilli, S. K.; Furtak, T. E.; Brown, L. D.; Deutsch, T. G.; Turner, J. A.; Herring, A. M. Cobalt-phosphate (Co-Pi) catalyst modified Mo-doped BiVO 4 photoelectrodes for solar water oxidation. *Energy Environ. Sci.* **2011**, *4* (12), 5028−5034.
(20) Jia, Y.; Wang, Z.; Ma, Y.; Liu, J.; Shi, W.; Lin, Y.; Hu, X.; Zhang, K. Boosting interfacial charge migration of TiO2/BiVO4 photoanode by W doping for photoelectrochemical water splitting. *Electrochim. Acta* **2019**, *300*, 138−144.
(21) Wang, W.; Strohbeen, P. J.; Lee, D.; Zhou, C.; Kawasaki, J. K.; Choi, K.-S.; Liu, M.; Galli, G. The role of surface oxygen vacancies in BiVO4. *Chem. Mater.* **2020**, *32* (7), 2899−2909.
(22) Wang, G.; Ling, Y.; Lu, X.; Qian, F.; Tong, Y.; Zhang, J. Z.; Lordi, V.; Rocha Leao, C.; Li, Y. Computational and photo-electrochemical study of hydrogenated bismuth vanadate. *J. Phys. Chem. C* **2013**, *117* (21), 10957−10964.
(23) Zhou, Y.; Zhang, L.; Lin, L.; Wygant, B. R.; Liu, Y.; Zhu, Y.; Zheng, Y.; Mullins, C. B.; Zhao, Y.; Zhang, X.; Yu, G. Highly efficient photoelectrochemical water splitting from hierarchical WO3/BiVO4 nanoporous sphere arrays. *Nano Lett.* **2017**, *17* (12), 8012−8017.
(24) Ge, G.; Liu, M.; Liu, C.; Zhou, W.; Wang, D.; Liu, L.; Ye, J. Ultrathin FeOOH nanosheets as an efficient cocatalyst for photo-catalytic water oxidation. *J. Mater. Chem. A* **2019**, *7* (15), 9222−9229.
(25) Zhang, X.; Li, H.; Kong, W.; Liu, H.; Fan, H.; Wang, M. Reducing the surface recombination during light-driven water oxidation by core-shell BiVO4@ Ni: FeOOH. *Electrochim. Acta* **2019**, *300*, 77−84.
(26) Rodríguez-Gutiérrez, I.; Djatoubai, E.; Rodríguez-Pérez, M.; Su, J.; Rodríguez-Gattorno, G.; Vayssieres, L.; Oskam, G. Photo-electrochemical water oxidation at FTO| WO3@ CuWO4 and FTO| WO3@ CuWO4| BiVO4 heterojunction systems: an IMPS analysis. *Electrochim. Acta* **2019**, *308*, 317−327.
(27) Xi, G.; Ye, J. Synthesis of bismuth vanadate nanoplates with exposed {001} facets and enhanced visible-light photocatalytic properties. *Chem. Commun.* **2010**, *46* (11), 1893−1895.
(28) Kim, C. W.; Son, Y. S.; Kang, M. J.; Kim, D. Y.; Kang, Y. S. (040)-Crystal Facet Engineering of BiVO4 Plate Photoanodes for Solar Fuel Production. *Adv. Energy Mater.* **2016**, *6* (4), No. 1501754.
(29) Lee, J. S.; Saroha, R.; Cho, J. S. Porous microspheres comprising CoSe2 nanorods coated with N-doped graphitic C and

polydopamine-derived C as anodes for long-lived Na-ion batteries. *Nano-Micro Lett.* **2022**, *14* (1), No. 113.
(30) Huang, Z.-F.; Pan, L.; Zou, J.-J.; Zhang, X.; Wang, L. Nanostructured bismuth vanadate-based materials for solar-energy-driven water oxidation: a review on recent progress. *Nanoscale* **2014**, *6* (23), 14044−14063.
(31) Zhong, M.; Hisatomi, T.; Kuang, Y.; Zhao, J.; Liu, M.; Iwase, A.; Jia, Q.; Nishiyama, H.; Minegishi, T.; Nakabayashi, M.; et al. Surface modification of CoO x loaded BiVO4 photoanodes with ultrathin p-type NiO layers for improved solar water oxidation. *J. Am. Chem. Soc.* **2015**, *137* (15), 5053−5060.
(32) Zachäus, C.; Abdi, F. F.; Peter, L. M.; Van De Krol, R. Photocurrent of BiVO 4 is limited by surface recombination, not surface catalysis. *Chem. Sci.* **2017**, *8* (5), 3712−3719.
(33) Zhong, D. K.; Choi, S.; Gamelin, D. R. Near-complete suppression of surface recombination in solar photoelectrolysis by "Co-Pi" catalyst-modified W: BiVO4. *J. Am. Chem. Soc.* **2011**, *133* (45), 18370−18377.
(34) Abdi, F. F.; Firet, N.; van de Krol, R. Efficient BiVO4 thin film photoanodes modified with Cobalt Phosphate catalyst and W-doping. *ChemCatChem* **2013**, *5* (2), 490−496.
(35) Nellist, M. R.; Qiu, J.; Laskowski, F. A.; Toma, F. M.; Boettcher, S. W. Potential-sensing electrochemical AFM shows CoPi as a hole collector and oxygen evolution catalyst on BiVO4 water-splitting photoanodes. *ACS Energy Lett.* **2018**, *3* (9), 2286−2291.
(36) Ding, C.; Shi, J.; Wang, D.; Wang, Z.; Wang, N.; Liu, G.; Xiong, F.; Li, C. Visible light driven overall water splitting using cocatalyst/BiVO 4 photoanode with minimized bias. *Phys. Chem. Chem. Phys.* **2013**, *15* (13), 4589−4595.
(37) Wang, S.; Chen, P.; Yun, J. H.; Hu, Y.; Wang, L. An electrochemically treated BiVO4 photoanode for efficient photoelectrochemical water splitting. *Angew. Chem.* **2017**, *129* (29), 8620−8624.
(38) Xue, D.; Kan, M.; Qian, X.; Zhao, Y. A tandem water splitting cell based on nanoporous BiVO4 photoanode cocatalyzed by ultrasmall cobalt borate sandwiched with conformal TiO2 layers. *ACS Sustainable Chem. Eng.* **2018**, *6* (12), 16228−16234.
(39) Choi, S. K.; Choi, W.; Park, H. Solar water oxidation using nickel-borate coupled BiVO 4 photoelectrodes. *Phys. Chem. Chem. Phys.* **2013**, *15* (17), 6499−6507.
(40) Kumar, S.; Satpati, A. K. Investigation of interfacial charge transfer kinetics of photocharged Co-Bi modified BiVO4 using scanning electrochemical microscopy (SECM). *Electrochim. Acta* **2021**, *368*, No. 137565.
(41) Novoselov, K. S.; Geim, A. K.; Morozov, S. V.; Jiang, D.-e.; Zhang, Y.; Dubonos, S. V.; Grigorieva, I. V.; Firsov, A. A. Electric field effect in atomically thin carbon films. *Science* **2004**, *306* (5696), 666−669.
(42) Novoselov, K. S.; Fal′ ko, V. I.; Colombo, L.; Gellert, P. R.; Schwab, M. G.; Kim, K. A roadmap for graphene. *Nature* **2012**, *490* (7419), 192−200.
(43) Tsang, A. C.; Kwok, H. Y.; Leung, D. Y. The use of graphene based materials for fuel cell, photovoltaics, and supercapacitor electrode materials. *Solid State Sci.* **2017**, *67*, A1−A14.
(44) Zhu, Y.; Murali, S.; Cai, W.; Li, X.; Suk, J. W.; Potts, J. R.; Ruoff, R. S. Graphene and graphene oxide: synthesis, properties, and applications. *Adv. Mater.* **2010**, *22* (35), 3906−3924.
(45) Liu, C.; Yu, Z.; Neff, D.; Zhamu, A.; Jang, B. Z. Graphene-based supercapacitor with an ultrahigh energy density. *Nano Lett.* **2010**, *10* (12), 4863−4868.
(46) Sharma, A.; Manna, S.; Satpati, A. K. Enhancement in Photoelectrochemical Efficiency and Modulation of Surface States in BiVO4 through the TiO2 Outer Layer Using the Atomic Layer Deposition Technique. *J. Phys. Chem. C* **2023**, *127* (9), 4395−4406.
(47) Meng, Q.; Zhang, B.; Fan, L.; Liu, H.; Valvo, M.; Edström, K.; Cuartero, M.; Marco, Rd.; Crespo, G. A.; Sun, L. Efficient BiVO 4 photoanodes by postsynthetic treatment: remarkable improvements in photoelectrochemical performance from facile borate modification. *Angew. Chem., Int. Ed* **2019**, *58* (52), 19027−19033.
(48) Wang, M.; Wang, Z.; Zhang, B.; Jiang, W.; Bao, X.; Cheng, H.; Zheng, Z.; Wang, P.; Liu, Y.; Whangbo, M.-H.; et al. Enhancing the photoelectrochemical water oxidation reaction of BiVO4 photoanode by employing carbon spheres as electron reservoirs. *ACS Catal.* **2020**, *10* (21), 13031−13039.
(49) Pelissari, M. R. d. S.; Azevedo Neto, N. F.; Camargo, L. P.; Dall'Antonia, L. H. Characterization and Photo-Induced Electrocatalytic Evaluation for BiVO4 Films Obtained by the SILAR Process. *Electrocatalysis* **2021**, *12* (3), 211−224.
(50) Sleight, A.; Chen, H.-y.; Ferretti, A.; Cox, D. E. Crystal growth and structure of BiVO4. *Mater. Res. Bull.* **1979**, *14* (12), 1571−1581.
(51) Galembeck, A.; Alves, O. BiVO4 thin film preparation by metalorganic decomposition. *Thin Solid Films* **2000**, *365* (1), 90−93.
(52) Yu, J.; Kudo, A. Hydrothermal synthesis of nanofibrous bismuth vanadate. *Chem. Lett.* **2005**, *34* (6), 850−851.
(53) Liu, J.; Wang, H.; Wang, S.; Yan, H. Hydrothermal preparation of BiVO4 powders. *Mater. Sci. Eng., B* **2003**, *104* (1−2), 36−39.
(54) Li, H.; Lin, H.; Xie, S.; Dai, W.; Qiao, M.; Lu, Y.; Li, H. Ordered mesoporous Ni nanowires with enhanced hydrogenation activity prepared by electroless plating on functionalized SBA-15. *Chem. Mater.* **2008**, *20* (12), 3936−3943.
(55) Ma, Z.; Liao, X.; Kong, G.; Chu, J. Raman scattering of nanocrystalline silicon embedded in SiO 2. *Sci. China, Ser. A: Math.* **2000**, *43*, 414−420.
(56) Adu, K. W.; Gutierrez, H. R.; Eklund, P. C. Raman-active phonon line profiles in semiconducting nanowires. *Vib. Spectrosc.* **2006**, *42* (1), 165−175.
(57) Richter, H.; Wang, Z.; Ley, L. The one phonon Raman spectrum in microcrystalline silicon. *Solid State Commun.* **1981**, *39* (5), 625−629.
(58) Tan, H. L.; Abdi, F. F.; Ng, Y. H. Heterogeneous photocatalysts: an overview of classic and modern approaches for optical, electronic, and charge dynamics evaluation. *Chem. Soc. Rev.* **2019**, *48* (5), 1255−1271.
(59) Wiktor, J.; Reshetnyak, I.; Ambrosio, F.; Pasquarello, A. Comprehensive modeling of the band gap and absorption spectrum of BiVO 4. *Phys. Rev. Mater.* **2017**, *1* (2), No. 022401.
(60) Walsh, A.; Yan, Y.; Huda, M. N.; Al-Jassim, M. M.; Wei, S.-H. Band edge electronic structure of BiVO4: elucidating the role of the Bi s and V d orbitals. *Chem. Mater.* **2009**, *21* (3), 547−551.
(61) Cooper, J. K.; Gul, S.; Toma, F. M.; Chen, L.; Liu, Y.-S.; Guo, J.; Ager, J. W.; Yano, J.; Sharp, I. D. Indirect bandgap and optical properties of monoclinic bismuth vanadate. *J. Phys. Chem. C* **2015**, *119* (6), 2969−2974.
(62) Cooper, J. K.; Gul, S.; Toma, F. M.; Chen, L.; Glans, P.-A.; Guo, J.; Ager, J. W.; Yano, J.; Sharp, I. D. Electronic structure of monoclinic BiVO4. *Chem. Mater.* **2014**, *26* (18), 5365−5373.
(63) JIANG, H.; Hongxing, D.; Xue, M.; ZHANG, L.; Jiguang, D.; Kemeng, J. Morphology-dependent photocatalytic performance of monoclinic BiVO4 for methyl orange degradation under visible-light irradiation. *Chin. J. Catal.* **2011**, *32* (6−8), 939−949.
(64) Pan, L.; Muhammad, T.; Ma, L.; Huang, Z.-F.; Wang, S.; Wang, L.; Zou, J.-J.; Zhang, X. MOF-derived C-doped ZnO prepared via a two-step calcination for efficient photocatalysis. *Appl. Catal., B* **2016**, *189*, 181−191.
(65) Liu, G.; Li, F.; Zhu, Y.; Li, J.; Sun, L. Cobalt doped BiVO 4 with rich oxygen vacancies for efficient photoelectrochemical water oxidation. *RSC Adv.* **2020**, *10* (48), 28523−28526.
(66) Idriss, H. On the wrong assignment of the XPS O1s signal at 531−532 eV attributed to oxygen vacancies in photo-and electro-catalysts for water splitting and other materials applications. *Surf. Sci.* **2021**, *712*, No. 121894.
(67) Henderson, M. A.; Perkins, C.; Engelhard, M. H.; Thevuthasan, S.; Peden, C. H. Redox properties of water on the oxidized and reduced surfaces of CeO2 (111). *Surf. Sci.* **2003**, *526* (1−2), 1−18.
(68) Shi, L.; Zhuo, S.; Abulikemu, M.; Mettela, G.; Palaniselvam, T.; Rasul, S.; Tang, B.; Yan, B.; Saleh, N. B.; Wang, P. Annealing temperature effects on photoelectrochemical performance of bismuth

https://doi.org/10.1021/acsomega.3c03229
ACS Omega 2023, 8, 33452−33465

vanadate thin film photoelectrodes. *RSC Adv.* **2018**, *8* (51), 29179−29188.
(69) Tafalla, D.; Salvador, P.; Benito, R. Kinetic approach to the photocurrent transients in water photoelectrolysis at n-TiO2 electrodes: II. Analysis of the photocurrent-time dependence. *J. Electrochem. Soc.* **1990**, *137* (6), 1810.
(70) Lee, M. G.; Yang, J. W.; Park, I. J.; Lee, T. H.; Park, H.; Cheon, W. S.; Lee, S. A.; Lee, H.; Ji, S. G.; Suh, J. M.; et al. Tailored BiVO4/In2O3 nanostructures with boosted charge separation ability toward unassisted water splitting. *Carbon Energy* **2023**, *5*, No. e321.
(71) Ye, H.; Park, H. S.; Bard, A. J. Screening of electrocatalysts for photoelectrochemical water oxidation on W-doped BiVO4 photocatalysts by scanning electrochemical microscopy. *J. Phys. Chem. C* **2011**, *115* (25), 12464−12470.
(72) Lee, M. G.; Yang, J. W.; Park, H.; Moon, C. W.; Andoshe, D. M.; Park, J.; Moon, C.-K.; Lee, T. H.; Choi, K. S.; Cheon, W. S.; et al. Crystal facet engineering of TiO2 nanostructures for enhancing photoelectrochemical water splitting with BiVO4 nanodots. *Nano-Micro Lett.* **2022**, *14* (1), 48.
(73) Lee, S. A.; Yang, J. W.; Lee, T. H.; Park, I. J.; Kim, C.; Hong, S. H.; Lee, H.; Choi, S.; Moon, J.; Kim, S. Y.; et al. Multifunctional nano-heterogeneous Ni (OH) 2/NiFe catalysts on silicon photoanode toward efficient water and urea oxidation. *Appl. Catal., B* **2022**, *317*, No. 121765.
(74) Mishra, G. K.; Kant, R. Modular theory for DC-biased electrochemical impedance response of supercapacitor. *J. Power Sources* **2020**, *473*, No. 228467.
(75) Kumar, R.; Kant, R. Experimental corroboration of general phenomenological theory for dynamics of EDL in viscous medium on rough heterogeneous electrode. *Electrochim. Acta* **2017**, *257*, 473−482.
(76) Park, H. S.; Ha, H.-W.; Ruoff, R. S.; Bard, A. J. On the improvement of photoelectrochemical performance and finite element analysis of reduced graphene oxide−BiVO4 composite electrodes. *J. Electroanal. Chem.* **2014**, *716*, 8−15.
(77) Gaikwad, M. A.; Ghorpade, U. V.; Suryawanshi, U. P.; Kumar, P. V.; Jang, S.; Jang, J. S.; Tran, L.; Lee, J.-S.; Bae, H.; Shin, S. W.; et al. Rapid Synthesis of Ultrathin Ni: FeOOH with In Situ-Induced Oxygen Vacancies for Enhanced Water Oxidation Activity and Stability of BiVO4 Photoanodes. *ACS Appl. Mater. Interfaces* **2023**, *15* (17), 21123−21133.
(78) Murugan, C.; Pandikumar, A. Reinforcement of Visible-Light Harvesting and Charge-Transfer Dynamics of BiVO4 Photoanode via Formation of p−n Heterojunction with CuO for Efficient Photoelectrocatalytic Water Splitting. *ACS Appl. Energy Mater.* **2022**, *5* (6), 6618−6632.
(79) Baral, B.; Parida, K. {040/110} Facet isotype heterojunctions with monoclinic scheelite BiVO4. *Inorg. Chem.* **2020**, *59* (14), 10328−10342.
(80) Murugan, C.; Ranjithkumar, K.; Pandikumar, A. Interfacial charge dynamics in type-II heterostructured sulfur doped-graphitic carbon nitride/bismuth tungstate as competent photoelectrocatalytic water splitting photoanode. *J. Colloid Interface Sci.* **2021**, *602*, 437−451.
(81) Baral, B.; Reddy, K. H.; Parida, K. Construction of M-BiVO4/T-BiVO4 isotype heterojunction for enhanced photocatalytic degradation of Norfloxacine and Oxygen evolution reaction. *J. Colloid Interface Sci.* **2019**, *554*, 278−295.
(82) Lewis, N. S. Chemical control of charge transfer and recombination at semiconductor photoelectrode surfaces. *Inorg. Chem.* **2005**, *44* (20), 6900−6911.
(83) Lewis, N. S. A Quantitative Investigation of the Open-Circuit Photovoltage at the Semiconductor/Liquid Interface. *J. Electrochem. Soc.* **1984**, *131* (11), 2496.
(84) Tan, M. X.; Kenyon, C.; Krüger, O.; Lewis, N. S. Behavior of Si photoelectrodes under high level injection conditions. 1. Steady-state current− voltage properties and quasi-Fermi level positions under illumination. *J. Phys. Chem. B* **1997**, *101* (15), 2830−2839.
(85) Krüger, O.; Kenyon, C.; Tan, M. X.; Lewis, N. S. Behavior of Si photoelectrodes under high level injection conditions. 2. Experimental measurements and digital simulations of the behavior of quasi-Fermi levels under illumination and applied bias. *J. Phys. Chem. B* **1997**, *101* (15), 2840−2849.
(86) Kenyon, C. N.; Tan, M. X.; Krüger, O.; Lewis, N. S. Behavior of Si photoelectrodes under high level injection conditions. 3. Transient and steady-state measurements of the quasi-Fermi levels at Si/CH3OH contacts. *J. Phys. Chem. B* **1997**, *101* (15), 2850−2860.
(87) Tan, M. X.; Kenyon, C.; Lewis, N. S. Experimental measurement of quasi-fermi levels at an illuminated semiconductor/liquid contact. *J. Phys. Chem. A* **1994**, *98* (19), 4959−4962.
(88) Walter, M. G.; Warren, E. L.; McKone, J. R.; Boettcher, S. W.; Mi, Q.; Santori, E. A.; Lewis, N. S. Solar water splitting cells. *Chem. Rev.* **2010**, *110* (11), 6446−6473.
(89) Chen, S.; Wang, L.-W. Thermodynamic oxidation and reduction potentials of photocatalytic semiconductors in aqueous solution. *Chem. Mater.* **2012**, *24* (18), 3659−3666.
(90) Hu, S.; Lewis, N. S.; Ager, J. W.; Yang, J.; McKone, J. R.; Strandwitz, N. C. Thin-film materials for the protection of semiconducting photoelectrodes in solar-fuel generators. *J. Phys. Chem. C* **2015**, *119* (43), 24201−24228.
(91) Gerischer, H. On the stability of semiconductor electrodes against photodecomposition. *J. Electroanal. Chem. Interfacial Electrochem.* **1977**, *82* (1−2), 133−143.

https://doi.org/10.1021/acsomega.3c03229
ACS Omega 2023, 8, 33452−33465